MDPI

Mechanism and Effect of the Dilution Gas Flow Rate on Various Fe–Si/SiO$_2$ Soft Magnetic Composites during Fluidised Bed Chemical Vapour Deposition

Zhaoyang Wu [1], **Zihan Gao [1]**, **Qian Zhao [1]**, **Hui Kong [2]**, **Mingyang Li [1,*]** and **Jixiang Jia [3,*]**

[1] Key Laboratory of Metallurgical Emission Reduction & Resources Recycling, Anhui University of Technology, Ma'anshan 243002, China; ahutwzy@ahut.edu.cn (Z.W.); zihanggg97@163.com (Z.G.); doczhaoqian@163.com (Q.Z.)

[2] International Science & Technology Cooperation Base for Intelligent Equipment Manufacturing under Special Work Environment, Anhui University of Technology, Ma'anshan 243002, China; konghui@ahut.edu.cn

[3] Ansteel Group, Ansteel Group Iron and Steel Research Institute, Anshan 114021, China

* Correspondence: my.l@ahut.edu.cn (M.L.); jjxman@sina.com (J.J.); Tel.: +86-0555-231-1571 (M.L.)

Abstract: The effect of the dilution gas flow rate on inorganic oxide insulating layers can improve fluidised bed chemical vapour deposition (FBCVD) in Fe–Si/inorganic-oxide soft magnetic composites and obtain excellent magnetic properties. Herein, Fe–Si/SiO$_2$ composite particles coated via FBCVD and deposited at a 125–350 mL/min Ar-dilution gas flow rate were prepared and sintered into soft magnetic composites. Results demonstrate that SiO$_2$ deposited on the Fe–Si substrate particle surface changed from submicron SiO$_2$ clusters (125 mL/min) to an incomplete SiO$_2$ film, then to a complete SiO$_2$ film, and finally to a porous SiO$_2$ film as the Ar-dilution gas flow rate increased. SiO$_2$ layers began to transform from the amorphous to the beta-cristobalite state with a hexagonal crystal structure between 1149.45 K and 1280.75 K. However, the SiO$_2$ amorphous layers' crystallisation did not affect the Fe–Si substrate particles' crystal structure. With the increasing Ar-dilution gas flow rate, the saturation magnetisation of Fe–Si/SiO$_2$ soft magnetic composites initially decreased and then increased. The electrical resistivity increased before 150 mL/min, followed by an increase between 150 and 250 mL/min and then decreased, whereas the total core loss exhibited the opposite trend. These results show that magnetic performance can be promoted by selecting a suitable dilution flow rate.

Keywords: dilution gas; soft magnetic composites; evolution mechanism; magnetic performance

1. Introduction

For advanced performance, as an energy conversion material in electromagnetic devices [1–3] and high-power high-frequency electrical devices [4], Fe–Si/inorganic-oxide soft magnetic composites have been studied by researchers worldwide. To coat an inorganic oxide insulating layer on Fe–Si magnetic particles, several methods, such as ball milling [5], mixed sintering [6], and the sol–gel process [7,8], were used to obtain Fe–Si/inorganic-oxide core–shell particles with high insulating quality. The disadvantage of these methods is the uncontrollability of homogeneity for the inorganic oxide-insulating layer. The fluidised bed chemical vapour deposition (FBCVD) method was first used to coat inorganic oxides on particles ~30 years ago [9]. Moreover, laboratory studies demonstrate that the FBCVD technique is a suitable and effective method for coating inorganic oxide-insulating layers on Fe–Si magnetic particles [10]. An 800-nm-thick inorganic oxide insulating layer can be deposited at a rate ranging between 4.2 and 17.6 nm/min on Fe–Si substrate particles [11].

The inorganic oxide-insulating layers are deposited on the particle surface by thermally decomposing the precursors [12–14]. However, during the subsequent particle-moulding process, the inorganic oxide-insulating layers easily break and collapse because of the large lattice mismatch and thermal expansion coefficient mismatch between inorganic oxides and

particle substrates [15,16], which may negatively impact performance. Therefore, research attention should be focused on the interfacial bonding between inorganic oxides and particle substrates and the compactness of the inorganic oxide-insulating layer's deposition. In the FBCVD system, multiple conditions, such as the deposition temperature, pressure, particle substrate size, precursor flow rate, and dilution gases, affect the deposition process and the properties of the final product. Recently, many studies have reported the effect of FBCVD process parameters on the quality of inorganic oxide deposition and related performance. Complete FBCVD experimental investigations were conducted to study the effect of the deposition time and the precursor's mole fraction on SnO_2 deposition with large hollow Ni particles [17]. To improve SiO_2 layer deposition using FBCVD, the effects of the deposition time and injection mode of SiH_4 on the deposition process were examined [18]. The effects of deposition temperature on the uniformity of the TiO_2 distribution of the Fe–Ni particles and photocatalysis were examined using the geometric limitation of real experiments [19]. Although these studies have significantly promoted research, the FBCVD experimental conditions on the compactness of inorganic oxide insulating layers deposited on the Fe–Si particle surface and the magnetic properties of Fe–Si/inorganic-oxide soft magnetic composites have not been reported thus far.

Herein, the impact of the Ar dilution gas flow rate on the microstructure of the SiO_2 layers deposited via FBCVD was examined. Further, the evolution mechanisms of SiO_2 layers under a series of Ar dilution gas flow rates are reported, and the effect of the magnetic properties of Fe–Si/SiO_2 soft magnetic composites is described. The results provide a certain basis for improving the Fe–Si/inorganic-oxide soft magnetic composites and process knowledge of FBCVD.

2. Materials and Methods

2.1. Materials

In this study, the substrate particles used were commercial gas-atomized Fe–Si particles with a particle size ranging between 45 and 90 μm. The nominal composition of the Fe–Si particles was Fe = 93.26, Si = 6.65, O = 0.02, C = 0. 07 (wt.%). Tetraethyl orthosilicate (National Medicine Group Chemical Reagent Co., Ltd., Shanghai, China) with a purity of 99.0 wt.% was selected as the SiO_2 precursor. Pure Ar gas (Nanjing Special Gas Plant Co. Ltd., Nanjing, China) with a purity of 99.999 wt.% was used as the dilution and carrier gas.

2.2. Preparation of Fe–Si/SiO_2 Composites Using FBCVD-HPS

Herein, Fe–Si/SiO_2 soft magnetic composites were fabricated through an FBCVD-hot press sintering (HPS) process, which involves two primary steps: (i) 50 g of Fe–Si particles was placed on a stainless steel strainer, with 30-μm-diameter pores, within a vertical tube furnace and fluidised using Ar dilution gas. Tetraethyl orthosilicate (outgassed at 423 K) was introduced into the furnace by another Ar carrier gas flow (at a rate of 100 mL/min) for 60 min when the furnace temperature reached 930 K. The Fe–Si/SiO_2 composite particles were collected after the furnace cooled to room temperature. (ii) Next, 26 g of Fe–Si/SiO_2 composite particles was packed into a graphite mould and sintered using an HPS condition (Hubei Changjiang Jinggong Material Technology Co. Ltd., Ezhou, China). The pressure was increased to 20 MPa, and then the temperature was increased to 1223 K in 10 min. The Fe–Si/SiO_2 soft magnetic composites were sintered at this temperature at a dwelling time of 10 min. The Fe–Si/SiO_2 composite particles and soft magnetic composites were adjusted by varying the flow rate of the Ar dilution gas from 125 to 350 mL/min.

2.3. Characterisation

The element distribution, surface, and cross-section morphologies of Fe–Si/SiO_2 composite particles and soft magnetic composites were characterised via scanning electron microscopy (SEM, Zeiss Sigma 300, Sigma, Ronkonkoma, NY, USA) and energy-dispersive spectrometry (EDS, OxfordX-MAX). A Bruker D8 Advance X-ray diffractometer (XRD, Bruker, Billerica, MA, USA), with CuKα radiation, was used to examine the phase com-

position of the synthesised Fe–Si/SiO$_2$ composite particles and soft magnetic composites. Furthermore, the changes in the crystal structure information, for the Fe–Si/SiO$_2$ soft magnetic composites during HPS, were obtained using Rietveld refinement. The Fe–Si/SiO$_2$ composite particles were thermally analysed via differential scanning calorimetry (DSC, Netasch 499C, Netzsch, Bavaria, Germany) at a heating rate of 10 K/min from 373.15 K to 1473.15 K under an argon atmosphere. The magnetic hysteresis loops of Fe–Si/SiO$_2$ soft magnetic composites were measured using a vibrating sample magnetometer (VSM, MPMS XL-7, Quantum Design, CA, USA) at room temperature with a maximum applied field of 20 kOe. Sheet resistances of the Fe–Si/SiO$_2$ soft magnetic composites were measured using a four-probe resistivity test system. The total core loss of Fe–Si/SiO$_2$ soft magnetic composites from 10 mT and 25–200 kHz, respectively, was examined using a B–H curve analyser (SY-8219, IWATSU, Tokyo, Japan).

3. Results

3.1. Morphology of Fe–Si/SiO$_2$ Composite Particles and Soft Magnetic Composites

The SEM and EDS mappings of the Fe–Si/SiO$_2$ composite particles were used to demonstrate the deposition of SiO$_2$ layers on Fe–Si substrate particles. The surface morphology of the Fe–Si/SiO$_2$ composite particles deposited at a flow rate of 250 mL/min for the Ar dilution gas is shown in Figure 1. The elemental signals of O obtained from the Fe–Si/SiO$_2$ composite particles are consistent with those of Fe and Si. The even distribution of these three elements indicates that an excellent and uniform SiO$_2$ layer can be deposited on the surface of the Fe–Si substrate particles through FBCVD. Figure 2 shows the surface morphologies of Fe–Si/SiO$_2$ composite particles obtained at various Ar dilution gas flow rates. Following FBCVD, compared with the clean and smooth surface of Fe–Si substrate particles seen in Figure S1, the surface of the Fe–Si/SiO$_2$ composite particles became rougher. Moreover, the particle surface morphology and SiO$_2$ layer quality were influenced by the flow rate of the Ar dilution gas. The submicron-sized SiO$_2$ clusters can be observed on the local areas of the sample surface when the flow rate of Ar dilution gas was relatively low (125 mL/min, Figure 2a), and the as-formed SiO$_2$ layer was unconnected. The deposited SiO$_2$ showed a decrease in the particle size, and its deposition changed from particles to a film as the flow rate of Ar dilution gas increased to 150 mL/min (Figure 2b). Moreover, the SiO$_2$ layers deposited on the surface of the Fe–Si substrate were evenly distributed at a flow rate of 200 mL/min of the Ar dilution gas, and the existing pits on the substrate surface were covered (Figure 2c). As the flow rate of the Ar dilution gas increased (Figure 2e), visible pores appeared among the SiO$_2$ layers, indicating that the homogeneity and compactness worsened at this stage. Furthermore, the cross-section backscattered images in Figure 2 confirmed that the Fe–Si/SiO$_2$ composite particles could be obtained at a gas flow rate of 125 mL/min for the Ar dilution gas; however, the optimal Ar dilution gas flow rate range for forming an integrated Fe–Si/SiO$_2$ core/shell heterostructure was between 200 and 300 mL/min. During FBCVD, the relationship between the deposition rate and Ar dilution gas flow rate can be obtained from the average thickness of the SiO$_2$ layers measured from the cross-section backscattered images using ImageJ software (shown in Figure 2g). The deposition rate for SiO$_2$ layers on the Fe–Si substrate particle surface initially increased from 2.20 (200 mL/min) to 9.70 nm/min (250 mL/min) and subsequently decreased to 2.68 nm/min (300 mL/min) after the integrated Fe–Si/SiO$_2$ core/shell heterostructure formed.

Figure 3a shows the SEM and EDS results of Fe–Si/SiO$_2$ soft magnetic composites sintered from the Fe–Si/SiO$_2$ composite particles deposited at an Ar dilution gas flow rate of 250 mL/min. A backscattered electron is sensitive to the mean atomic number of the material: the larger the mean atomic number, the brighter the corresponding backscattered electron image. The elemental distribution signal shows that the Fe element was mainly concentrated in the inner Fe–Si particle area. The O element was distributed at the interface between the Fe–Si particles, indicating that the Fe–Si/SiO$_2$ soft magnetic composites featured a core/shell heterostructure with a SiO$_2$ layer shell and an Fe–Si-particle core. The

detected backscattered high-energy electrons in Figure 3c–h indicate the evolution of the cross-section morphology for the Fe–Si/SiO$_2$ soft magnetic composites from an Ar dilution gas flow rate of 125–350 mL/min. The Fe–Si compacts in Figure 3b showed a smooth polished surface without defects or air gaps, indicating a high density and mechanical strength. However, the uneven SiO$_2$ layers with several pores can be observed in the cross-sections of Fe–Si/SiO$_2$ soft magnetic composites deposited at an Ar dilution gas flow rate of 125 mL/min. A small portion of the interface between the Fe–Si particles became difficult to distinguish. The uniformity, continuity, and average thickness of SiO$_2$ layers increased and the interface between the Fe–Si particles became more distinct when the Ar dilution gas flow rate increased from 125 to 250 mL/min. However, with increase in the Ar dilution gas flow rate from 300 to 350 mL/min, the inhomogeneous phenomenon of SiO$_2$ layers reappeared. Furthermore, the mean thickness of the SiO$_2$ layers decreased.
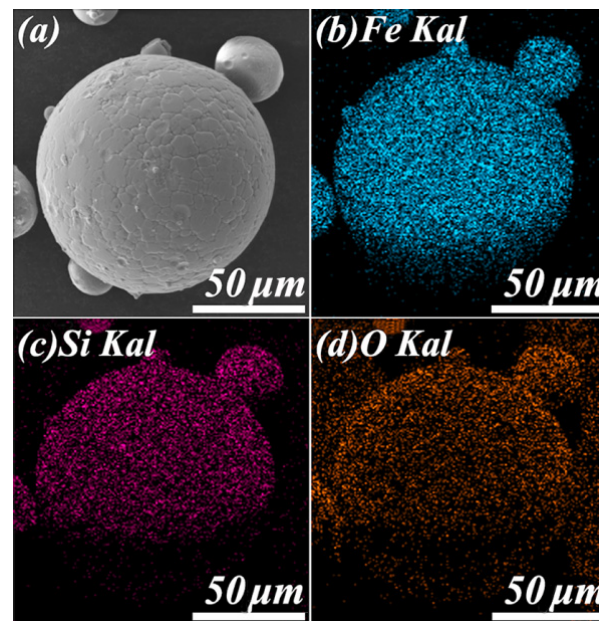
Figure 1. (**a**) SEM morphology of Fe–Si/SiO$_2$ composite particles deposited at an Ar dilution gas flow rate of 250 mL/min and elemental distribution images of Fe (**b**), Si (**c**), and O (**d**).
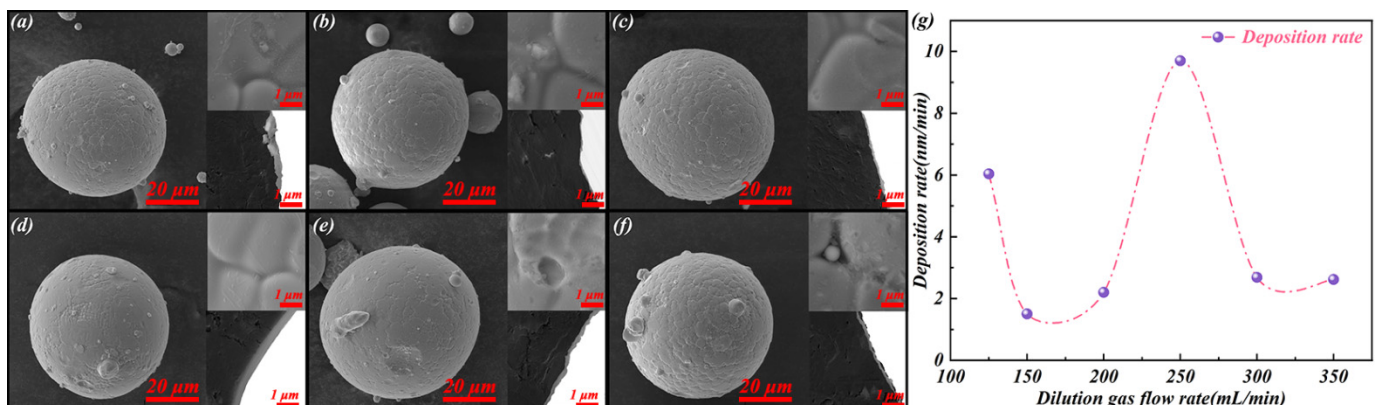
Figure 2. Surface morphology, partial enlargement morphology, and cross-sectional morphology of Fe–Si/SiO$_2$ composite particles deposited at 125 (**a**), 150 (**b**), 200 (**c**), 250 (**d**), 300 (**e**), and 350 (**f**) mL/min Ar-dilution gas flow rate; (**g**) SiO$_2$ layer deposition rate of particles prepared at various Ar-dilution gas flow rates.
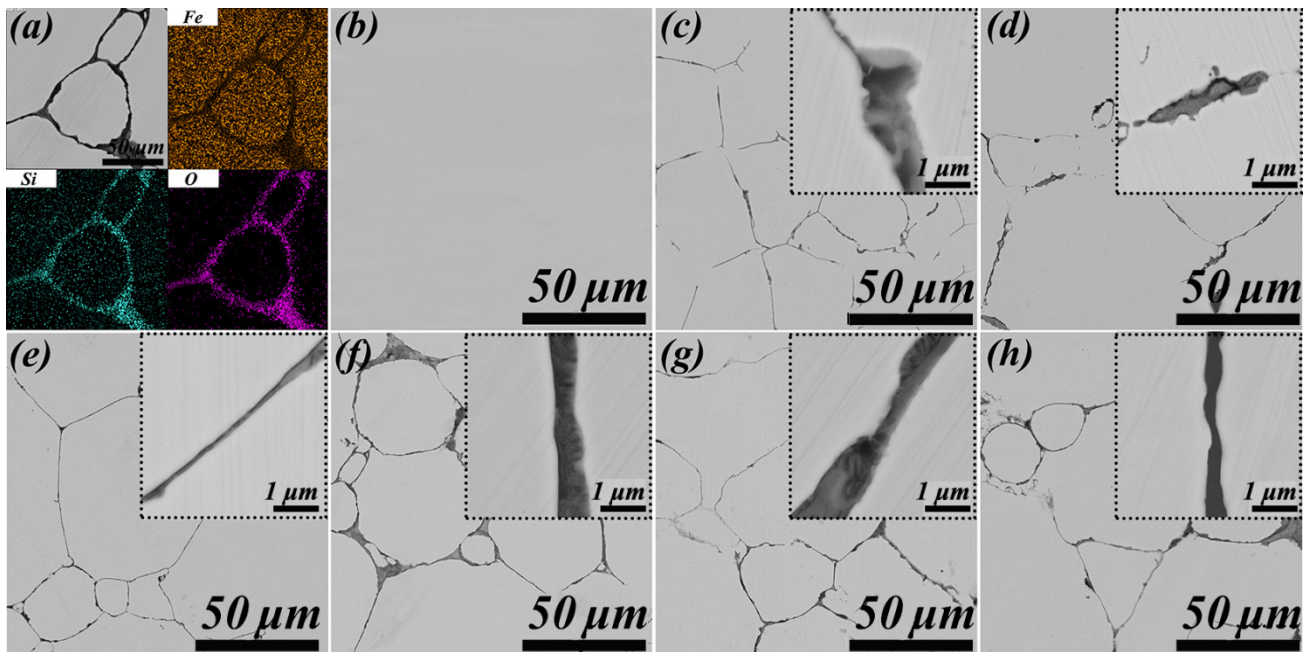
Figure 3. (**a**) EDS Fe, Si and O maps of Fe–Si/SiO$_2$ soft magnetic composites deposited at an Ar-dilution gas flow rate of 250 mL/min. Backscattered electron images of Fe–Si compacts (**b**) and Fe–Si/SiO$_2$ soft magnetic composites deposited at an Ar-dilution gas flow rate of (**c**) 125, (**d**) 150, (**e**) 200, (**f**) 250, (**g**) 300, and (**h**) 350 mL/min.
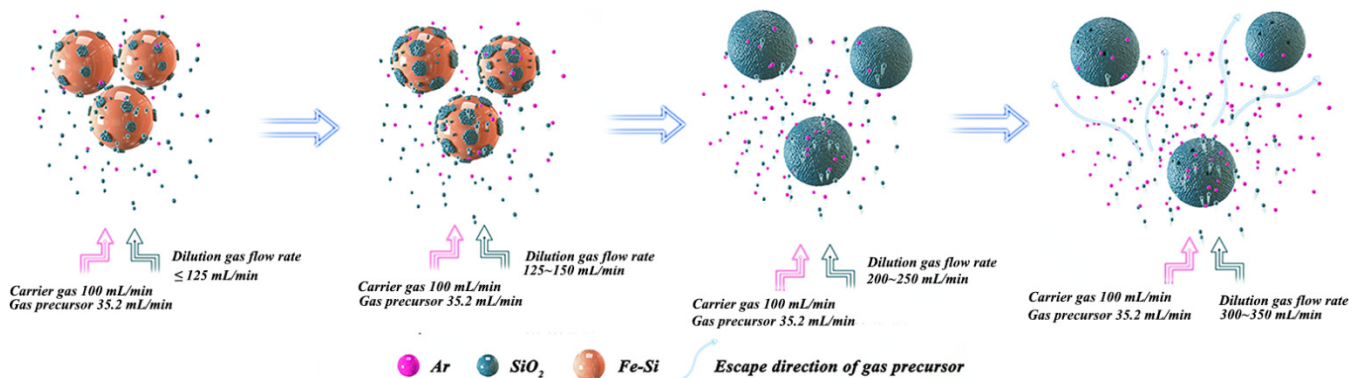
3.2. Influential Mechanism of the Ar-Dilution Gas Flow Rate

Based on the typical fluidisation behaviour of Geldart-B particles [20], the gas flow rate (V_{Ar}) of Ar gas, which contacts with the Fe–Si substrate particles, and the initial fluidisation velocity ($V_{Fe(Si)}$) of Fe–Si substrate particles can be expressed as follows:

$$V_{Ar} = \frac{(V_{Ar1} + V_{Ar2}) \times 10^{-6}}{60 \times \pi r^2} \tag{1}$$

$$V_{Fe(Si)} = \frac{d^2(\rho_{Fe(Si)} - \rho_{Ar})g}{1650 \times \mu_{Ar}}, \tag{2}$$

where V_{Ar1} and V_{Ar2} are the flow rates of the Ar dilution and carrier gases, respectively (mL/min). r is the radius of the stainless steel strainer (m); d is the particle size of the Fe–Si substrate particles (m); $\rho_{Fe(Si)}$ and ρ_{Ar} are the densities of Fe–Si substrate particles and Ar gas, respectively (kg/m^3); g is the acceleration because of gravity (N/kg); and μ_{Ar} is the viscosity of Ar gas (Pa·s). To maintain Fe–Si substrate particles in a fluidised condition during FBCVD, the V_{Ar} should exceed $V_{Fe(Si)}$. Figure 4 shows the schematic of the possible influential mechanism of the Ar-dilution gas flow rate on the microscopic appearances of Fe–Si/SiO$_2$ composite particles. In this study, the gasflow status in the reaction during FBCVD was determined by the flow rate of the Ar dilution gas. Under the condition that the partial pressure of the gaseous SiO$_2$ precursor was maintained constant in the experimental system, the Ar-dilution gas flow rate corresponded to a variation in gasflow boundary layer thickness. The SiO$_2$ layers on the Fe–Si/SiO$_2$ composite particle surface changed with the flow rate of the Ar dilution gas as follows.

Figure 4. Schematic of a possible influential mechanism of the Ar-carrier gas flow rate on the microscopic appearances of Fe–Si/SiO$_2$ composite particles.

1. When the Ar dilution gas flow is relatively low (125 mL/min), the dynamic viscosity of Ar gas increases with the reaction temperature, although V_{Ar} before the reaction is greater than $V_{Fe(Si)}$. The Fe–Si substrate particles cannot continue to maintain fluidisation and the gas SiO$_2$ precursor contacts with the partial surface of accumulated Fe–Si substrate particles. At this stage, the SiO$_2$ deposition presents submicron clusters.

2. As the Ar dilution gas flow rate increases to 150 mL/min, the Fe–Si substrate particles break away from the state of being unable to fluidise because of high temperature, and the gas SiO$_2$ precursor passes through the substrate particles. However, the content of the gas SiO$_2$ precursor in the reaction system is less because of the low flow rate of the Ar dilution gas. The submicron SiO$_2$ clusters transition towards incomplete and uneven SiO$_2$ layers. Simultaneously, the deposition rate of the SiO$_2$ layers drops.

3. When the Ar-dilution gas flow rate increases to some extent (200 and 250 mL/min), the Ar dilution gas can maintain the Fe–Si substrate particles in a fluidised suspension motion despite the increase in temperature during the deposition reaction. The gaseous SiO$_2$ precursor is uniformly distributed on the surface of the Fe–Si substrate particles. According to the theory of sedimentary process [21], Ar gas functions as a carrier and dilute gas precursor, belonging to quality transport control. The diffusion resistance of the gaseous SiO$_2$ precursor through the gasflow boundary layer decreases with in the increasing Ar-dilution gas flow rate. Thus, the number of gas–solid collisions and the reaction rate at the gas–solid interface are increased by decreasing the occurrence of homogenous gas-nucleation reactions before contact with the Fe–Si substrate particle surface. As the Ar dilution gas flow rate increases, the SiO$_2$ layer deposition rate increases. SiO$_2$ layers exist in the form of a coated film.

4. However, as the Ar-dilution gas flow rate continues to increase (300 and 350 mL/min), the excessive Ar dilution gas flow, at this time, reduces the diffusion resistance of the gaseous SiO$_2$ precursor, the retention time of the gaseous SiO$_2$ precursor in the vertical tube furnace, and the effective reaction time with the Fe–Si substrate particle surface. Certain gaseous SiO$_2$ precursors are expelled with the Ar dilution gas prior to deposition, and the high gas flow rate will reduce the temperature around the Fe–Si substrate particles. The deposition rate of the SiO$_2$ layer at this Ar-dilution gas flow rate decreases owing to the reduced reaction rate at the gas–solid interface. Thus, surface defects, such as holes, appear in the SiO$_2$ layers.

3.3. Crystal Structure Evolution during HPS

Figure 5a shows the XRD pattern of the Fe–Si/SiO$_2$ composite particles deposited at a Ar carrier gas flow rate of 250 mL/min. The observed peaks at 44.8°, 65.2°, and 82.6° indexed as (110), (200), and (211) agree with the α-Fe(Si) solid-solution (JCPDS file No. 3-065-6323). One extra amorphous peak arose at ~22°, indicating that the SiO$_2$ layer is amorphous. An ultra-low intensity diffraction peak located at 26.6° appeared in the Fe–

Si/SiO$_2$ soft magnetic composites (Figure 5b), corresponding to the (011) plane of the SiO$_2$ crystal phase (JCPDS file No. 1-070-2517). The results show that SiO$_2$ layers crystallised during HPS. Furthermore, the XRD experimental results were refined using Fullprof to estimate the effect of the crystallisation of amorphous SiO$_2$ layers on the crystal structure of the Fe–Si substrate particles [22]. Table 1 lists the crystal refinement data. The low values for R_{wp} (weighted peak residual variance factor), R_p (peak residual variance factor), and S (fitting degree) indicate that the Rietveld calculations are consistent with the experimental results. The additional SiO$_2$ crystal phase in the Fe–Si/SiO$_2$ soft magnetic composites was arranged in a hexagonal crystal structure, in which the ratio of the vertical cell (c) to the bottom cell (a) parameters was 1.368. Herein, the experimental conditions were maintained in the thermodynamically stable region of tridymite (monoclinic system); however, this contradicts the XRD results. This phenomenon can be interpreted using Ostwald's step rule [23,24], which states that the beta-cristobalite mesophase (hexagonal system) appears during the transformation from amorphous SiO$_2$ to the thermodynamic-stable phase (quartz or tridymite). However, the amorphous SiO$_2$ first converted to beta-cristobalite, and then to quartz or tridymite. The long-term and stable existence of beta-cristobalite is attributed to the different rate constants of these two reactions. The rate constant of the former reaction is larger than that of the latter reaction. In the above-mentioned two reactions, the new phase is formed via the destruction and reconstruction of the Si–O bond, which requires high activation energy. However, in practice, the formation conditions of beta-cristobalite are benign because the free energy difference between beta-cristobalite and quartz or tridymite is low and even <10 kJ/mol with amorphous SiO$_2$ [25]. It can be hypothesised that the dynamic disordered structure of beta-cristobalite is similar to the medium-range ordered structure of amorphous SiO$_2$, increasing the reaction rate of the transformation from amorphous SiO$_2$ to beta-cristobalite. Therefore, the crystalline structure of beta-cristobalite can be detected rather than that of the thermodynamically stable tridymite after amorphous SiO$_2$ crystallisation occurring at the temperature range in this study. However, cell parameters ($a = b = c = 2.859$ Å) of the body-centred cubic α-Fe(Si) phase in the Fe–Si/SiO$_2$ soft magnetic composites are almost identical to those in the Fe–Si/SiO$_2$ composite particles. The schematic of the crystal structure of Fe–Si/SiO$_2$ composite particles and soft magnetic composites were drawn using Vesta [26] based on the structural parameters, after refinement in Figure 5c. The results show that the crystallisation of SiO$_2$ layers can occur during HPS but does not influence the crystal structure of Fe–Si substrate particles. To demonstrate the thermal effect and temperature range for the crystallisation of SiO$_2$ layers, Figure 5d shows the DSC curve and the relative crystallinity as a function of the temperature of Fe–Si/SiO$_2$ composite particles. The DSC result shows that the SiO$_2$ layers transformed from the amorphous to the beta-cristobalite state between 1149.45 K and 1280.75 K. Furthermore, the crystallinity of Fe–Si/SiO$_2$ composite particles rose before 1226.05 K, which is attributed to the increase in crystal nuclei number. Then, with an increase in temperature, the crystallisation rate curve tended to be relatively flat and became smooth at 1280.75 K.

3.4. Magnetic Behaviour of Fe–Si/SiO$_2$ Soft Magnetic Composites

Figure 6 shows the magnetic hysteresis curves of Fe–Si compacts and Fe–Si/SiO$_2$ soft magnetic composites sintered from the composite particles deposited at different Ar-dilution gas flow rates. The saturation magnetisation and the coercivity of Fe–Si compacts reached 195.9 emu/g and 11 Oe, respectively. However, all saturation magnetisation values decreased in Fe–Si/SiO$_2$ soft magnetic composites compared with Fe–Si compacts, and the saturation magnetisation of Fe–Si/SiO$_2$ soft magnetic composites initially decreased and then increased with the increase in the Ar-dilution gas flow rate, thus exhibiting a trend opposite to that of the deposition rate of the SiO$_2$ layers. This trend is attributed to the Fe–Si/SiO$_2$ soft magnetic composites, which are equivalent to the introduction of non-magnetic SiO$_2$ into the Fe–Si compacts, wherein the number of non-magnetic SiO$_2$ first increased and then decreased with the increase in the Ar-dilution gas flow rate, thus

varying the magnetic moment ratio of magnetic materials. Therefore, during FBCVD, Fe–Si/SiO$_2$ soft magnetic composites with different saturation magnetisation values can be obtained by controlling the Ar-dilution gas flow rate. However, the coercivity of magnetic materials is an inherent property influenced by the number and strength of magnetic dipole moments and the interaction between adjacent magnetic domains. No difference was observed between the Fe–Si/SiO$_2$ soft magnetic composites and the Fe–Si compacts, indicating that the non-magnetic SiO$_2$ layers and Fe–Si/SiO$_2$ core–shell structures affected the magnetic domain.

Table 1. Crystal refinement data of Fe–Si/SiO$_2$ composite particles and soft magnetic composites.

	Refinement Parameters			**Phase**	**Cell Parameters**			**Bond Angle**		
	R_{wp}	R_p	S		a	b	c	α	β	γ
Fe–Si/SiO$_2$ composite particles	5.58%	4.18%	2.36	Fe–Si	2.859	2.859	2.859	90.00	90.00	90.00
Fe–Si/SiO$_2$ soft magnetic composites	5.96%	4.37%	2.78	Fe–Si	2.859	2.859	2.859	90.00	90.00	90.00
				SiO$_2$	5.041	5.041	5.253	90.00	90.00	120.00
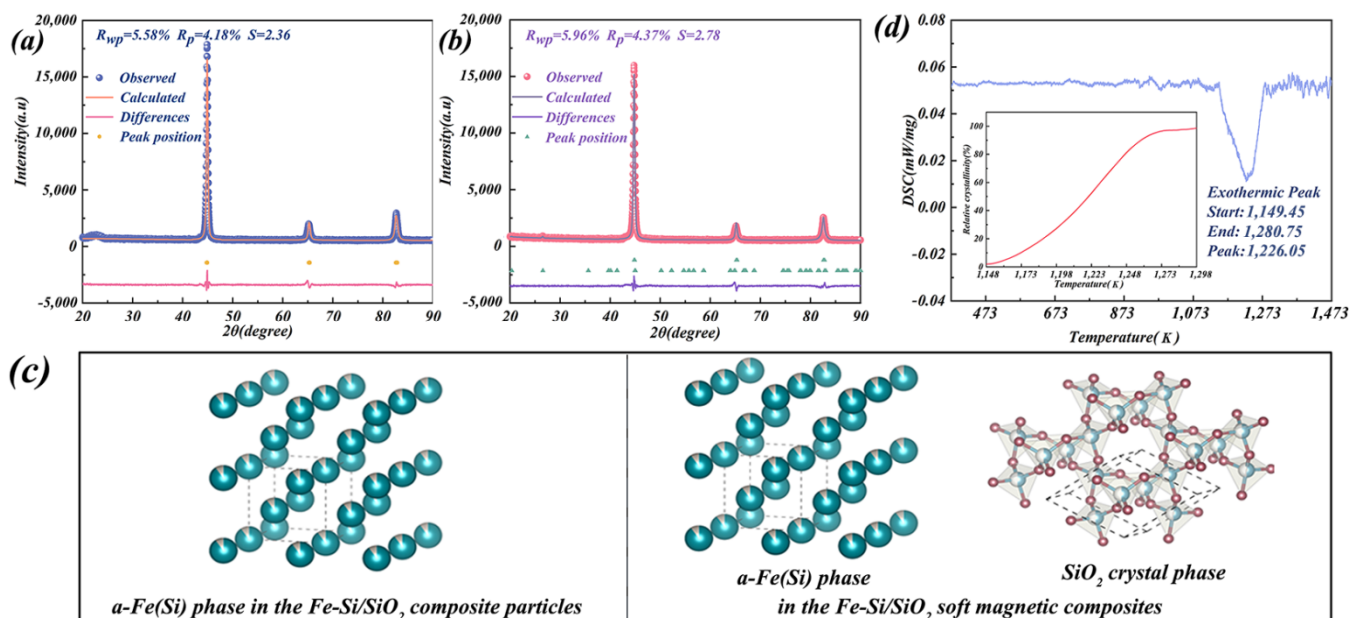
Figure 5. Rietveld refinement patterns of XRD data for (**a**) Fe–Si/SiO$_2$ composite particles and (**b**) soft magnetic composites; (**c**) schematics of the crystal structure of Fe–Si/SiO$_2$ composite particles and soft magnetic composites; (**d**) DSC curves and relative crystallinity, as a function of temperature, for Fe–Si/SiO$_2$ composite particles.

Figure 7 shows the measured results of the bulk material's electrical resistivity for Fe–Si compacts and Fe–Si/SiO$_2$ soft magnetic composites. According to the permeability theory, the introduction of SiO$_2$ layers with high resistivity (10^{11}–10^{13} $\mu\Omega\cdot$cm) into the Fe–Si compacts will increase the distance between conductive Fe–Si particles and destroy the continuous and dense conductive network formed by the conductive Fe–Si particles, thereby increasing the electron tunnelling barrier and reducing the electron tunnelling probability. Therefore, all Fe–Si/SiO$_2$ soft magnetic composites had higher electrical resistivity values than the Fe–Si compacts (Figure 7). The electrical resistivity of Fe–Si/SiO$_2$ soft magnetic composites increased before 150 mL/min, followed by a rapid increase between 150 and 250 mL/min and then decreased. This result can be explained by combining with the possible influential mechanism of the Ar-dilution gas flow rate on the microstructure of Fe–Si/SiO$_2$ composite particles (Figure 4). The electrical resistivity of Fe–Si/SiO$_2$ soft magnetic composites was affected by contact with the conductive Fe–Si particles and the distance between conductive Fe–Si particles. SiO$_2$ is deposited on the surface of Fe–Si substrate particles in the form of molecules, one by one, during FBCVD. SiO$_2$ deposition

on the surface of Fe–Si substrate particles is accompanied by several surface defects when the Ar dilution gas flow is relatively low; thus, the conductive Fe–Si particles can directly contact and generate a slow increase in electrical resistivity. SiO_2 layers existed in the form of a complete film as the Ar-dilution gas flow rate increased to 150 mL/min. The vacancies filled up, and the conductive Fe–Si particles were no longer contacted. However, the distance between Fe–Si particles increased with the increasing thickness of the SiO_2 layer; thus, the electrical resistivity rapidly increased. However, because the Ar-dilution gas flow rate continued to increase, the surface defects, such as holes, appeared in SiO_2 layers and the conductive Fe–Si particle contact; thus, the electrical resistivity began to decrease.
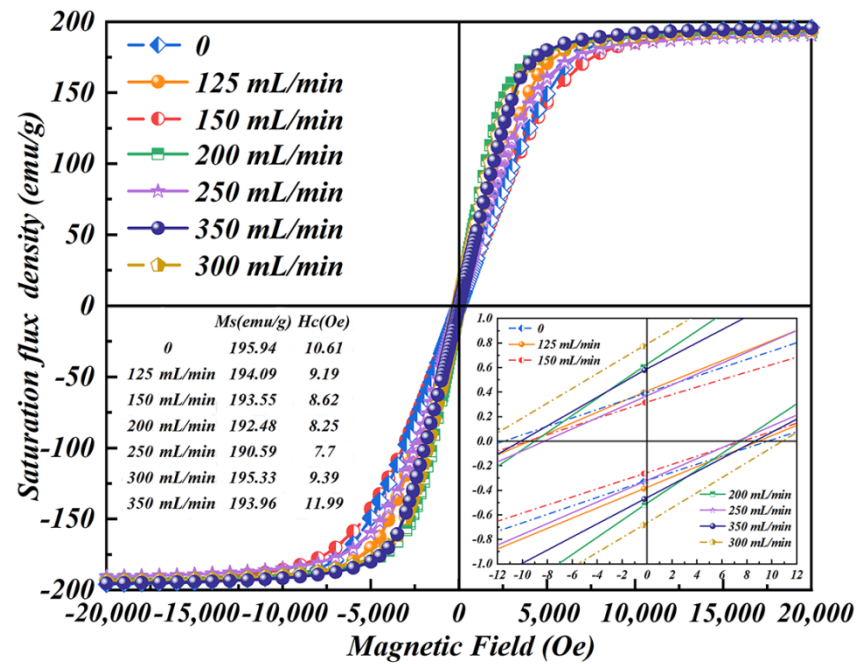

Figure 6. Magnetic hysteresis and partial enlarged curves of Fe–Si compacts and Fe–Si/SiO_2 soft magnetic composites at different Ar-dilution gas flow rates.
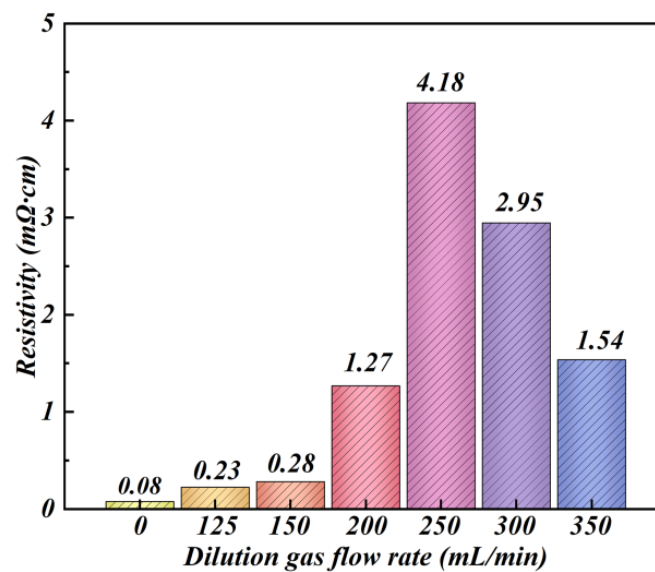

Figure 7. Bulk material's electrical resistivity for Fe–Si compacts and Fe–Si/SiO_2 soft magnetic composites.

The total core loss (W_{cv}, W/kg) was a magnetic parameter for the Fe–Si compacts and Fe–Si/SiO$_2$ soft magnetic composites used in the power application. Table 2 lists W_{cv} measured at 10 mT and 50–200 kHz for the Fe–Si compacts and Fe–Si/SiO$_2$ soft magnetic composites deposited at various Ar-dilution gas flow rates. With increasing measurement frequency and maximum magnetic flux density, W_{cv} demonstrated a persistent increasing trend for the Fe–Si/SiO$_2$ soft magnetic composites. Moreover, we observed that the W_{cv} of Fe–Si/SiO$_2$ soft magnetic composites decreased slowly as the Ar-dilution gas flow rate increased and then rapidly decreased and finally increased. When the Ar-dilution gas flow rate reached 250 mL/min, the W_{cv} of Fe–Si/SiO$_2$ soft magnetic composites was 215.7 W/kg, which was 51.0% lower than the Fe–Si compacts at 200 kHz. This can be attributed to the superior resistivity of the SiO$_2$ layer, limiting eddy current losses at high frequencies.

Table 2. Comparison of the total core loss of Fe–Si compacts and Fe–Si/SiO$_2$ soft magnetic composites.

Samples	Ar Dilution Gas Flow Rate (mL/min)	Total Core Loss (W/kg)				
		$W_{10/25}$	$W_{10/50}$	$W_{10/100}$	$W_{10/150}$	$W_{10/200}$
Fe–Si compacts	0	19.8	54.6	151.4	274.1	423.2
Fe–Si/SiO$_2$ composite compacts	125	19.5	53.9	150.7	225.5	275.8
	150	15.6	42.8	119	215.9	271.2
	200	13.9	39.1	108.1	197.4	259.3
	250	11.0	30.7	83.7	152.7	215.7
	300	11.4	31.9	90.6	169.5	221.5
	350	13.9	38.3	106.4	192.1	232.5

4. Conclusions

FeSi/SiO$_2$ soft magnetic composites were fabricated via FBCVD and HPS technologies. The mechanism of the microstructural evolution of SiO$_2$ layers, under a series of Ar-dilution gas flow rates and its effect on magnetic properties of Fe–Si/SiO$_2$ soft magnetic composites, was examined. The results in this study can be summarized as follows.

- With an increase in the Ar-dilution gas flow rate from 125 to 350 mL/min during FBCVD, SiO$_2$ deposited on the Fe–Si substrate particle surface presented the microscopic characteristics of "sub-micron SiO$_2$ clusters (125 mL/min) → incomplete SiO$_2$ layers (150 mL/min) → complete SiO$_2$ film (200 and 250 mL/min) → porous SiO$_2$ film (300 and 350 mL/min)".
- The dynamic disordered structure of beta-cristobalite was similar to the medium-range ordered structure of amorphous SiO$_2$, increasing the reaction rate of the transformation from amorphous SiO$_2$ to beta-cristobalite. Thus, SiO$_2$ layers transformed from the amorphous to the beta-cristobalite state with a hexagonal crystal structure at 1226.05 K during HPS. However, the crystallisation of SiO$_2$ layers did not affect the crystal structure of Fe–Si substrate particles.
- The saturation magnetisation of Fe–Si/SiO$_2$ soft magnetic composites initially decreased and then increased with increasing Ar-dilution gas flow rate. The electrical resistivity of Fe–Si/SiO$_2$ soft magnetic composites slowly increased before 150 mL/min, followed by a rapid increase, between 150 and 250 mL/min, and then decreased while the total core loss exhibited the opposite trend. The lowest total core loss value (215.7 W/kg) was observed at the Ar-dilution gas flow rate of 250 mL/min.

The results pave the way for the efficient production of the Fe–Si/inorganic-oxide soft magnetic composites and provide a certain basis for improving FBCVD technology.

References

1. Shokrollahi, H.; Janghorban, K. Soft magnetic composite materials (SMCs). *J. Mater. Process. Technol.* **2007**, *189*, 1–12. [CrossRef]
2. Vijayakumar, K.; Thiagarajan, Y.; Rajendirakumar, R.; Basanth, A.J.; Karthikeyan, R.; Kannan, S. Development of an iron powder metallurgy soft magnetic composite core switched reluctance motor. *Mater. Today Proc.* **2021**, *41*, 1195–1201.
3. Talaat, A.; Suraj, M.V.; Byerly, K.; Wang, A.; Wang, Y.; Lee, J.K.; Ohodnicki, P.R. Review on soft magnetic metal and inorganic oxide nanocomposites for power applications. *J. Alloys Compd.* **2021**, *870*, 159500. [CrossRef]
4. Svensson, L.; Frogner, K.; Jeppsson, P.; Cedell, T.; Andersson, M. Soft magnetic moldable composites: Properties and applications. *J. Magn. Magn. Mater.* **2012**, *324*, 2717–2722. [CrossRef]
5. Wu, Z.; Fan, X.; Jian, W.; Li, G.; Zhang, Z. Core loss reduction in Fe–6.5 wt.%Si/SiO$_2$ core–shell composites by ball milling coating and spark plasma sintering. *J. Alloys Compd.* **2014**, *617*, 21–28. [CrossRef]
6. Gheisari, K.; Javadpour, S.; Shokrollahi, H.; Hashemi, B. Magnetic losses of the soft magnetic composites consisting of iron and Ni–Zn ferrite. *J. Magn. Magn. Mater.* **2008**, *320*, 1544–1548. [CrossRef]
7. Clapsaddle, B.J.; Gash, A.E.; Satcher, J.H.; Simpson, R.L. Silicon oxide in an iron(III) oxide matrix: The sol–gel synthesis and characterization of Fe–Si mixed oxide nanocomposites that contain iron oxide as the major phase. *J. Non-Cryst. Solids* **2003**, *331*, 190–201. [CrossRef]
8. Zhou, B.; Dong, Y.; Chi, Q.; Zhang, Y.; Chang, L.; Gong, M.; Huang, J.; Pan, Y.; Wang, X. Fe-based amorphous soft magnetic composites with SiO$_2$ insulation coatings: A study on coatings thickness, microstructure and magnetic properties. *Ceram. Int.* **2020**, *46*, 13449–13459. [CrossRef]
9. Aizawa, T.; Ito, M.; Kihara, J. Acoustic diagnosis for nondestructive evaluation of ceramic coatings on the steel substrates. *Am. Soc. Mech. Eng.* **1995**, *302*, 257–270.
10. Wu, Z.Y.; Jiang, Z.; Fan, X.A.; Zhou, L.J.; Wang, W.L.; Xu, K. Facile synthesis of Fe-6.5wt%Si/SiO$_2$ soft magnetic composites as an efficient soft magnetic composite material at medium and high frequencies. *J. Alloys Compd.* **2018**, *742*, 90–98. [CrossRef]
11. Liu, L.; Liao, X.W.; Jia, J.X.; Kong, H.; Fan, X.A.; Wu, Z.Y.; Wang, X.S. Temperature-controlled conversion from Fe–Si particles to integrated Fe–Si/SiO$_2$ core–shell structure particles during fluidised bed chemical vapour deposition. *Ceram. Int.* **2020**, *46*, 3059–3065. [CrossRef]
12. Labropoulos, A.I.; Romanos, G.E.; Karanikolos, G.N.; Katsaros, F.K.; Kakizis, N.K.; Kanellopoulos, N.K. Comparative study of the rate and locality of silica deposition during the CVD treatment of porous membranes with TEOS and TMOS. *Microporous Mesoporous Mater.* **2009**, *120*, 177–185. [CrossRef]
13. Baux, A.; Jacques, S.; Allemand, A.; Vignoles, G.L.; David, P.; Piquero, T.; Stempin, M.P.; Chollon, G. Complex geometry macroporous SiC ceramics obtained by 3D-printing, polymer impregnation and pyrolysis (PIP) and chemical vapor deposition (CVD). *J. Eur. Ceram. Soc.* **2021**, *41*, 3274–3284. [CrossRef]
14. Bain, M.F.; Low, Y.H.; Bien, D.C.S.; Montgomery, J.H.; Armstrong, B.M.; Gamble, H.S. Investigation into the selectivity of CVD iron from Fe(CO)5 precursor on various metal and dielectric patterned substrates. *Surf. Coat. Technol.* **2007**, *201*, 8998–9002. [CrossRef]

15. Vlasenko, V.G.; Zubkov, S.V.; Shuvaeva, V.A.; Abdulvakhidov, K.G.; Shevtsova, S.I. Crystal structure and dielectric properties of aurivillius phases A 0.5 Bi 4.5 B 0.5 Ti 3.5 O 15 (A = Na, Ca, Sr, Pb; B = Cr, Co, Ni, Fe, Mn, Ga). *Physics Solid State* **2014**, *56*, 1554–1560. [CrossRef]

16. Zhang, S.; Hattori, N.; Enomoto, M.; Tarui, T. Ferrite Nucleation at Ceramic/Austenite Interfaces. *ISIJ Int.* **1996**, *36*, 1301–1309. [CrossRef]

17. Bertrand, N.; Maury, F.; Duverneuil, P. SnO2 coated Ni particles prepared by fluidized bed chemical vapor deposition. *Surf. Coat. Technol.* **2006**, *200*, 6733–6739. [CrossRef]

18. Cadoret, L.; Rossignol, C.; Dexpert-Ghys, J.; Caussat, B. Chemical vapor deposition of silicon nanodots on TiO_2 submicronic powders in vibrated fluidized bed. *Mater. Sci. Eng. B* **2010**, *170*, 41–50. [CrossRef]

19. Ma, L.; Chen, A.; Lu, J.; Zhang, Z.; He, H.; Li, C. In situ synthesis of CNTs/Fe–Ni/TiO2 nanocomposite by fluidized bed chemical vapor deposition and the synergistic effect in photocatalysis. *Particuology* **2014**, *14*, 24–32. [CrossRef]

20. Amarasinghe, W.S.; Jayarathna, C.K.; Ahangama, B.S.; Tokheim, L.A.; Moldestad, B.M.E. Experimental Study and CFD Modelling of Minimum Fluidization Velocity for Geldart A, B and D Particles. *Int. J. Modeling Optim.* **2017**, *7*, 152–156. [CrossRef]

21. Grabke, H.J.; Moszynski, D.; Müller-Lorenz, E.; Schneider, A. Role on sulfur in carburization, carbide formation and metal dusting on iron. *Surf. Interface Anal.* **2010**, *34*, 369–374. [CrossRef]

22. Frontera, C.; Rodríguez-Carvajal, J. FullProf as a new tool for flipping ratio analysis: Further improvements. *Phys. B Condens. Matter* **2004**, *350*, E731–E733. [CrossRef]

23. Nordeng, S.H.; Sibley, D.F. Dolomite stoichiometry and Ostwald's Step Rule. *Geochim. Cosmochim. Acta* **1994**, *58*, 191–196. [CrossRef]

24. Morse, J.W.; Casey, W.H. Ostwald processes and mineral paragenesis in sediments. *Am. J. Sci.* **1988**, *288*, 537–560. [CrossRef]

25. Berman, R.G. Internally-Consistent Thermodynamic Data for Minerals in the System Na_2O-K_2O-CaO-MgO-FeO-Fe_2O_3-Al_2O_3-SiO_2-TiO_2-H_2O-CO_2. *J. Petrol.* **1988**, *29*, 445–522. [CrossRef]

26. Momma, K.; Izumi, F. VESTA: A three-dimensional visualization system for electronic and structural analysis. *J. Appl. Crystallogr.* **2008**, *41*, 653–658. [CrossRef]